Surface engineered PdNFe₃ intermetallic electrocatalyst for boosting oxygen reduction in alkaline media

Jiamin Liu [a,1], Longhai Zhang [a,1], Jiaye Liu [b], Zhihang Xu [d], Jiaxi Zhang [a], Lecheng Liang [a], Li Du [a], Huiyu Song [a], Ye Zhu [d], Nanwen Li [c], Zhiming Cui [a,*]

[a] *The Key Laboratory of Fuel Cell Technology of Guangdong Province, School of Chemistry and Chemical Engineering, South China University of Technology, Guangzhou 510641, China*
[b] *College of Chemical & Pharmaceutical Engineering, Hebei University of Science & Technology, Shijiazhuang 050018, China*
[c] *State Key Laboratory of Coal Conversion, Institute of Coal Chemistry, Chinese Academy of Sciences, Taiyuan 030001, China*
[d] *Department of Applied Physics, Research Institute for Smart Energy, The Hong Kong Polytechnic University, 999077, Hong Kong Special Administrative Region*

ARTICLE INFO

ABSTRACT

Surface engineering has been identified as an effective way to maximize the utilization of noble atoms and facilitate the oxygen reduction reaction. However, a cost-effective and highly durable platform for tailoring the electrocatalytic activity, is still absent. Herein, we demonstrate a new and promising catalytic material of antiperovskite-typed PdNFe₃ and construct a high performance PdNFe₃@Pd catalyst with atomic layers of strained Pd shell. The PdNFe₃@Pd/C catalyst presents a high mass activity (MA) of 1.14 A mg_{Pd}^{-1} at 0.9 V, which is 9 and 6 times higher than those of the Pt/C and Pd/C, respectively. More importantly, the excellent performance of PdNFe₃@Pd/C was also verified in anion-exchange membrane fuel cells and rechargeable Zn−air batteries. Density functional theory calculations reveal that the strain effect aroused by the lattice mismatch between PdNFe₃ core and Pd shell contributes to the enhanced ORR performance by optimizing the binding strength of oxygen intermediates on Pd.

1. Introduction

The oxygen reduction reaction (ORR) in alkaline media is an essential half-reaction in many energy storage and conversion systems, including rechargeable metal-air batteries and anion exchange membrane fuel cells (AEMFCs). The ORR in alkaline media has many advantages as compared with acid media, including the faster oxygen reduction reaction kinetics, less corrosive environments, and more importantly allowing for the use of Pt-free catalysts [1–4]. Among the developed alternatives to Pt-based catalysts, palladium (Pd), with relatively high abundance and comparable activity to Pt, has gained enormous research attentions and been considered as promising alternative to Pt catalysts [5]. Tremendous efforts have been devoted to improving the electrocatalytic performances of Pd-based catalysts by various strategies such as size and shape control [6–8], alloying with transition metals and heteroatom doping [9–11]. In spite of remarkable progresses, none of the reported Pd-based catalysts have advanced far enough to synchronously meet all the requirements of activity,

durability and cost for fuel cell cathode catalysts. Therefore, it is highly desirable and essential to explore high-performance and low-cost Pd-based catalysts for substantially enhancing ORR in alkaline media.

Surface engineering, such as constructing core−shell structure, has been identified as a powerful and feasible strategy for optimizing the catalytic performance as well as maximizing the utilization of precious metals [12–15]. The core−shell nanocatalysts are generally synthesized by either covering Pd shell on a proper core, or surface de-alloying of Pd-based alloys [10,16,17]. The interaction between core substrate and Pd shell can tune the binding strength of intermediates on Pd surface, thus boosting the ORR activity [10,14]. The element composition of cores/supports has critical impact on the lattice spacing/strain state of the shell as well as the total cost of the catalysts. So far, core substrates are mainly made of noble metals or Pd-based alloys with a high content of Pd, which leads to high cost [14,18]. In addition, the Pd-based alloys usually suffer from a substantial leaching of the less noble metals during long-term ORR electrocatalysis. Intermetallic compounds with atomically ordered structures, have emerged as a class of promising

electrocatalysts for the ORR [19–21]. In particular, less noble metals in intermetallic nanoparticles (NPs) possess high leaching tolerance owing to the stronger heteroatomic bond and a more negative enthalpy of formation compared to disordered alloys [22,23]. However, previous studies on intermetallic catalysts mainly focus Pt-based intermetallic system with very few reports on Pd-based intermetallic compounds, not to mention low Pd intermetallic catalysts [22,24,25]. Compared to Pd_3M and PdM (M = transition metal) intermetallics, PdM_3 type intermetallic nanocrystals have lower Pd content, but are thermodynamically unstable because of their positive formation energy. For example, Jain et al. performed the theoretical calculation revealing that the formation energy of $L1_2$-$PdFe_3$ intermetallics are 0.067 eV/atom, suggesting an unfavorable phase. Interestingly, the nitriding of $L1_2$-$PdFe_3$ to antiperovskite $PdNFe_3$ can greatly lower the formation energy (−0.198 eV/atom). Such phenomenon is also observed on other antiperovskite nitrides such as $PdNMn_3$ (−0.301 eV/atom) and $PdNCr_3$ (−0.247 eV/atom), indicating that antiperovskite $PdNM_3$ possess thermodynamically favorable structures [26]. Apparently, Pd-based antiperovskite nitrides, featuring low cost, well-defined composition and structure, represent a class of ideal core material for rational design of high-performance core−shell catalysts for ORR in alkaline media.

To verify our hypothesis, we selected $PdNFe_3$ as core substrate for constructing atomic layers of strained Pd shell by chemical dealloying and annealing processes. The obtained core–shell $PdNFe_3$@Pd electrocatalyst exhibits over 9-fold enhancement in mass activity and specific activity compared with commercial Pt/C catalyst toward ORR at 0.9 V_{RHE}. More importantly, the excellent performance of $PdNFe_3$@Pd/C was also verified in anion-exchange membrane fuel cells and rechargeable Zn−air batteries. The enhanced mechanism of $PdNFe_3$@Pd/C is revealed by density functional theory (DFT) calculations.

2. Experimental section

2.1. Chemicals

Palladium(II) acetylacetonate ($Pd(NO_3)_2$·2 H_2O, Pd ≥ 39.0%) and Iron(III) nitrate nonahydrate ($Fe(NO_3)_3$·9 H_2O, 99.9%) were purchased from Aladdin Ltd. Ketjenblack Carbon was purchased from Suzhou Yilongsheng Energy Tech Co., Ltd. Pt/C (20 wt%) was purchased from Johnson Matthey Chemicals Ltd. All chemicals were used as received primordially without further purification.

2.2. Preparation of PdNFe₃@Pd/C antiperovskite nitride

The carbon-supported $PdNFe_3$/C nanoparticles were prepared using a freeze-drying method, followed by a high-temperature post treatment and dealloyed by chemical leaching as follows. First, 0.040 mmol of Pd $(NO_3)_2$·2 H_2O and 0.120 mmol of $Fe(NO_3)_3$·9 H_2O were dissolved in deionized water, and 40 mg of Ketjen-300 J carbon support were dispersed in it. A well-dispersed slurry was obtained with ultrasonication for 2 h and was then dried through a freeze-drying process (24 h). Subsequently, the products were calcined at 600 °C under a flow of NH_3 for 6 h at a heating rate of 2 °C min^{-1} to obtain $PdNFe_3$/C. Then, the powders were thoroughly washed in 1 mol L^{-1} acetic acid aqueous solutions for 12 h to remove parts of Fe that was on their surface, followed by annealing under 95% Ar + 5% H_2 at 200 °C for 2 h, giving $PdNFe_3$@Pd/C catalyst for further study.

2.3. Preparation of 20 wt% Pd/C catalyst

The contrast catalyst of Pd/C for electrochemical measurements was synthesized via a similar method. In a typical process, 40 mg of Ketjen-300 J support and 0.094 mmol $Pd(NO_3)_2$·2 H_2O were dispersed in deionized water and then was ultrasonication for 1 h to obtain a well-dispersed slurry. Subsequently, the mixture was dried through freeze-drying (24 h). The final product was obtained by annealing under

95% Ar + 5% H_2 at 300 °C for 2 h.

2.4. Material characterization

The phase purity and crystallinity of the products were identified by X-ray powder diffraction (XRD) on a Rigaku MiniFlex 600 diffractometer with Cu Kα radiation (λ = 0.15406 nm). Transmission electron microscopy (TEM) was performed with a FEI TF20. HRTEM imaging was carried out on a FEI-Titan ST electron microscope operated at 300 kV. High angle annular dark-field (HAADF) characterization combined with energy-dispersive X-ray spectroscopy (EDS) mapping collection was conducted with a double aberration-corrected scanning transmission electron microscope (STEM) Spectra 300 operated at accelerating voltage of 300 kV and equipped with Super-X EDS spectrometer. X-ray photoelectron spectroscopy (XPS) analysis was conducted on the Thermo Scientific K-Alpha employing monochromated Al-Ka X-ray sources (hv=1486.6 eV). Inductively coupled plasma mass spectrometry (ICP-MS) data was measured on an Agilent 7800.

2.5. Electrochemical measurements

All the electrochemical tests were performed on an Autolab Electrochemical Instrumentation (Metrohm) with a conventional three-electrode system. A Pt wire and Hg/HgO (1.0 M KOH) electrode respectively served as the counter and reference electrodes, and the working electrode was a glassy carbon electrode (GC, 0.196 cm^2), which was modified with different electrocatalysts. 5 mg as-synthesized catalysts were dispersed in the mixture containing 850 μL isopropanol, 100 μL H_2O and 50 μL of 5 wt% Nafion solution to form the homogeneous catalyst ink by sonicating for 50 min. Then 4 μL of the dispersion was drop-casted on the disk electrode respectively and dried at room temperature to yield a thin-film electrode. ORR measurements were conducted in a 0.1 M KOH solution purged with oxygen during the measurement. The scan rate and rotation rate for ORR measurement were 10 mV s^{-1} and 1600 rpm. The yield of H_2O_2 and the electron transfer number (n) are calculated by referring to the following equation: in which i_d and i_r indicate the disk current and the ring current, N stands for current collection efficiency of the RRDE (N = 0.37).

$$y_{H_2O_2} = \frac{200i_r}{Ni_d + i_r} \quad n = \frac{4Ni_d}{Ni_d + i_r}$$

The electrochemically active surface area (ECSA) of Pd-based materials were determined by CO-stripping, assuming a charge density of 420 μC per cm^{-2} $_{Pd}$. First, CO gas (99.99%) was bubbled into the electrolyte (0.1 M KOH) with holding the working electrode potential at 0.1 V versus RHE for 15 min; N_2 was then purged the above electrolyte to remove CO for at least 30 min. Two cyclic voltammograms were recorded at a scan rate of 25 mV s^{-1}. The ECSA was calculated by integrating the charge of CO stripping (the first cyclic voltammogram) after the background charge (the second cyclic voltammogram) subtraction. The ECSA of Pt/C was measured by hydrogen adsorption/desorption method in alkaline conditions. The tests were conducted in argon-saturated 0.1 M KOH aqueous solution. A continuous steam of argon was introduced into the cell for 30 min above the liquid surface to maintain an inert atmosphere.

2.6. Alkaline anion exchange membrane fuel cells test

The performance of the $PdNFe_3$@Pd/C was conducted under AEMFCs conditions. Specifically, $PdNFe_3$@Pd/C was employed as the cathode catalysts, and Pt/C (40 wt% loading, Johnson Matthey) was used for the anode. The catalyst was mixed with isopropanol, deionized water, and anion exchange ionomer, and then was ultrasonically dispersed for 1 h to prepare the ink and sprayed directly onto anion exchanged membrane (AEM) with a fixed catalyst coating area of 5 cm^2. The cathode and anode loadings are 0.5 mg cm^{-2}. The H_2−O_2 fuel cell
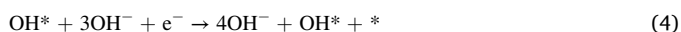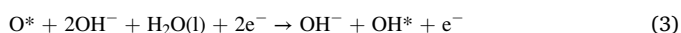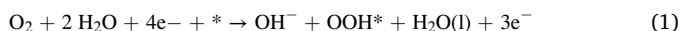
was tested on a SMART2PEMDM fuel cell test bench with 60 °C cell temperature, 1000 mL/min gas flow rate for H_2 and O_2, 1.0 bar back-pressure, and 100% relative humidity. The AEM was modified from previously reported work [27].

2.7. Theoretical calculation methods

The density of states (DOS) and Gibbs reaction free energy of each ORR elementary step were computed using the Vienna Ab initio Simulation Package (VASP) [28]. Projector augmented wave (PAW) and the generalized gradient approximation (GGA) with the Perdew-Burke-Ernzerhof (PBE) functional were used to describe the ion-electron interaction and the exchange-correlation potential [29,30]. The cutoff energy was set to be 450 eV while the convergence threshold for the self-consistent field (SCF) and ion steps were set to be 1×10^{-5} eV and 0.03 eV $Å^{-1}$. Spin polarization was considered in all computations. The slabs containing six closed-packed layers were build, in which the bottom two layers were fixed. The vacuum space of all investigated slab models was set to be 15 Å to eliminate the interaction between neighboring slabs. For structure optimization and DOS calculation, $4 \times 4 \times 1$ and $9 \times 9 \times 1$ Monkhorst-Pack sampled k-points were used respectively [31]. The overall ORR in an alkaline environment is:

$$O_2 + 2 H_2O + 4e^- \rightarrow 4OH^-.$$
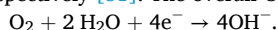
which can be divided into four elementary steps as follows [32]:

$$O_2 + 2 H_2O + 4e- + * \rightarrow OH^- + OOH* + H_2O(l) + 3e^- \quad (1)$$

$$OOH* + OH^- + H_2O(l) + 3e^- \rightarrow 2OH^- + O* + H_2O(l) + 2e^- \quad (2)$$

$$O* + 2OH^- + H_2O(l) + 2e^- \rightarrow OH^- + OH* + e^- \quad (3)$$

$$OH* + 3OH^- + e^- \rightarrow 4OH^- + OH* + * \quad (4)$$

For each step, * represents the adsorption site. The reaction free energy ΔG_1, ΔG_2, ΔG_3 and ΔG_4 is defined as follows [33]:

$$\Delta G = \Delta E + \Delta ZPE - T\Delta S - eU$$

in which ΔE is the DFT calculated reaction energy, ΔZPE represents the change in zero-point energy, ΔS represents the change in entropy and U represents the equilibrium potential. The equilibrium potential for ORR was determined to be 0.46 V vs NHE. in 0.1 M KOH.

The formation energies (E_f) for alloys (A_xB_y) and nitride (A_xB_yN) were calculated as follows:

$$E_f(A_xB_y)=E(A_xB_y)-xE(A)-yE(B)$$

$$E_f(A_xB_yN)=E(A_xB_yN)-xE(A)-yE(B)-E(N)$$

where $E(A_xB_y)$ and $E(A_xB_yN)$ are the calculated energies of A_xB_y and A_xB_yN, $E(A)$, $E(B)$, and $E(N)$ are the calculated energies of metal A, metal B and the N atom, x and y are the stoichiometric ratio.

3. Results and discussion

Carbon supported $PdNFe_3$ was synthesized by an impregnation–reduction method: the uniform dispersion of metal precursors on Ketjen-300 J carbon support by a freeze-drying method, and the subsequent annealing process under a flow of NH_3 at 600 °C. The experimental details are presented in the Experimental sections. Fig. 1a shows X-ray diffraction (XRD) patterns of carbon supported $PdNFe_3$ ($PdNFe_3$/ C). The distinct diffraction peaks at 23.0°, 32.76°, 40.42°, 47.02° and 68.68° can be assigned to the (100), (110), (111), (200) and (220) of the typical antiperovskite $PdNFe_3$ (ICSD 97–005–3506) with a *Pm3m* space group [34–37]. Very interestingly, when the N in the $PdNFe_3$ crystals was removed by annealing in a reductive atmosphere (H_2/Ar), the final sample formed mixed phases of metallic Fe and $L1_0$-PdFe instead of the ordered $PdFe_3$ (Fig. S1a). When the mixed phases are re-annealed in NH_3 atmosphere, antiperovskite $PdNFe_3$ is formed again (Fig. S1b). Besides, heat treatment of the metal salt precursors at different temperatures under H_2/Ar flow was conducted to form the $PdFe_3$ intermetallic. Unfortunately, the precursors were gradually reduced to form the mixed
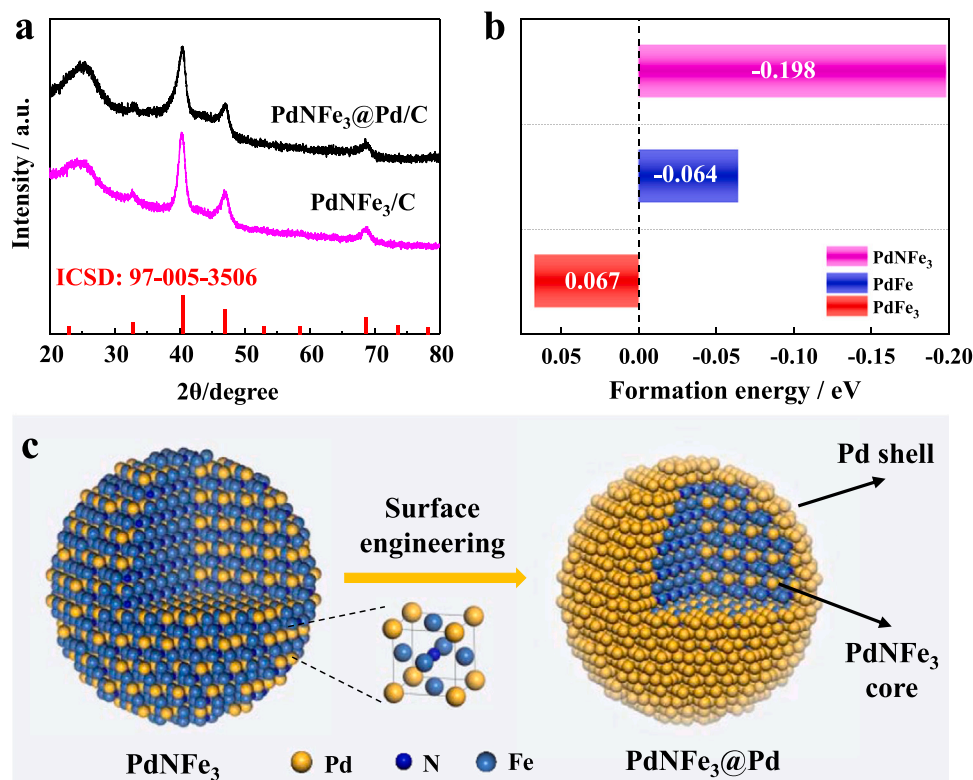

Fig. 1. (a) XRD patterns of $PdNFe_3$/C and $PdNFe_3$ @Pd/C; (b) Bulk formation energy of antiperovskite $PdNFe_3$, ordered PdFe and $PdFe_3$; (c) Schematic diagram of surface engineering on $PdNFe_3$.

phases of Fe and ordered $L1_0$-PdFe with the increment of temperatures (Fig. S2a-c). This indicates that a mixed phase of $L1_0$-PdFe and Fe is thermodynamically favorable in Pd-Fe$_3$ system. DFT calculations were carried out to reveal the origin of the superior structural stability of PdNFe$_3$ [26]. As shown in Fig. 1b, the formation energy of the PdNFe$_3$ is much lower than that of the PdFe and PdFe$_3$, suggesting that PdNFe$_3$ is thermodynamically favourable phase. Combining the experimental and theoretical analysis, antiperovskite-type PdNFe$_3$ is a more suitable platform/core material than PdFe$_3$ and PdFe to construct the low-Pd and core-shell structured catalyst.

To construct a Pd shell on PdNFe$_3$, as shown in Fig. 1c, the as-synthesized PdNFe$_3$/C was treated with mild acetic acid to remove the Fe at the surface, and subsequently annealed under a H$_2$/Ar atmosphere to form PdNFe$_3$ @Pd/C catalyst with atomic layers of strained Pd shell. As shown in Fig. 1a, the XRD peaks of the PdNFe$_3$ @Pd/C show slightly broader feature compared to the PdNFe$_3$/C after the surface dealloying, which can be ascribed of the decrease of the crystallinity by the leaching of the surface Fe. This is consistent with the literature where the surface dealloying would decrease the crystallinity of the intermetallic electrocatalyst [38]. Besides, the diffraction peaks of PdNFe$_3$ @Pd/C are slightly asymmetry due to the lattice mismatch between fct-PdNFe$_3$ core and fcc-Pd shell [39].

Fig. 2a and b show the TEM images of PdNFe$_3$/C and PdNFe$_3$ @Pd/C, respectively. It can be observed that both PdNFe$_3$ NPs and PdNFe$_3$ @Pd NPs are uniformly dispersed on carbon support with no obvious agglomeration and have a narrow size distribution. The average size of the PdNFe$_3$ @Pd NPs, as estimated from histograms (Fig. S3d), is approximately 6 nm in diameter. Fig. S4a shows the atomic resolution STEM image of a PdNFe$_3$. The ordered bright columns and dark columns are of Pd atoms and Fe atoms, as smiualted in Fig. S4b. Fig. S4c shows the corresponding FFT image, with the presence of superlattice reflections such as (001) and (110), proving the ordered structure of

antiperovskite PdNFe$_3$. The crystalline nature of PdNFe$_3$ @Pd/C is further confirmed by high resolution TEM (HRTEM). As shown in Fig. 2c, an interplanar spacing of 0.223 nm is observed, which can be indexed to the (111) plane of PdNFe$_3$ antiperovskite. The spatial distributions of Pd and Fe in PdNFe$_3$ @Pd were resolved by EDS-mapping (Fig. 2d). According to the mapping data, the Fe atoms were mainly distributed in the core, while the Pd atoms were evenly distributed across the whole nanoparticle,

confirming the formation of a core-shell structure. The EDS-line profile shows a typical Pd shell thickness of ~0.5 nm (Fig. 2e), which is roughly equivalent to 2–3 at. layers of Pd. The formation of a smooth Pd skin on the PdNFe$_3$ can also be confirmed by its cyclic voltammogram (CV) behavior. CV curves of PdNFe$_3$/C and PdNFe$_3$ @Pd/C at a sweep rate of 100 mV s^{-1} were collected in N$_2$-saturated 0.1 M HClO$_4$ solution. As shown in Fig. 2f, the current aroused by the typical hydrogen adsorption/desorption behaviour at platinum group metals cannot be detected in the CV curve of PdNFe$_3$/C, indicating a very low Pd content on the surface of the pristine PdNFe$_3$ NPs. In contract, PdNFe$_3$ @Pd/C catalyst exhibits obvious Pd features in the adsorption/desorption of hydrogen region, confirming the formation of a Pd shell on PdNFe$_3$ NPs. The X-ray photoelectron spectra (XPS) analysis was further employed to analyze the near-surface chemical environment of as-prepared PdNFe$_3$ @Pd/C. As shown in Fig. S5a, the full XPS spectrum confirms the presence of Pd, Fe and N peaks. The N 1 s spectra of PdNFe$_3$ @Pd/C (Fig. S5b) could be attributed to the oxidized N, graphitic N, pyrrolic N, pyridinic N and metal-N, respectively [40]. The exsistence of graphitic N, pyrrolic N and pyridinic N indicates the formation of N-doped C after NH$_3$-atmophsphere annealing. The strong metal-N signal proves the exsistence of N in the crystal lattice. The actual Pd loading in PdNFe$_3$ @Pd/C is 8.2 wt%, analyzed by inductively coupled plasma atomic emission spectroscopy (ICP-AES).

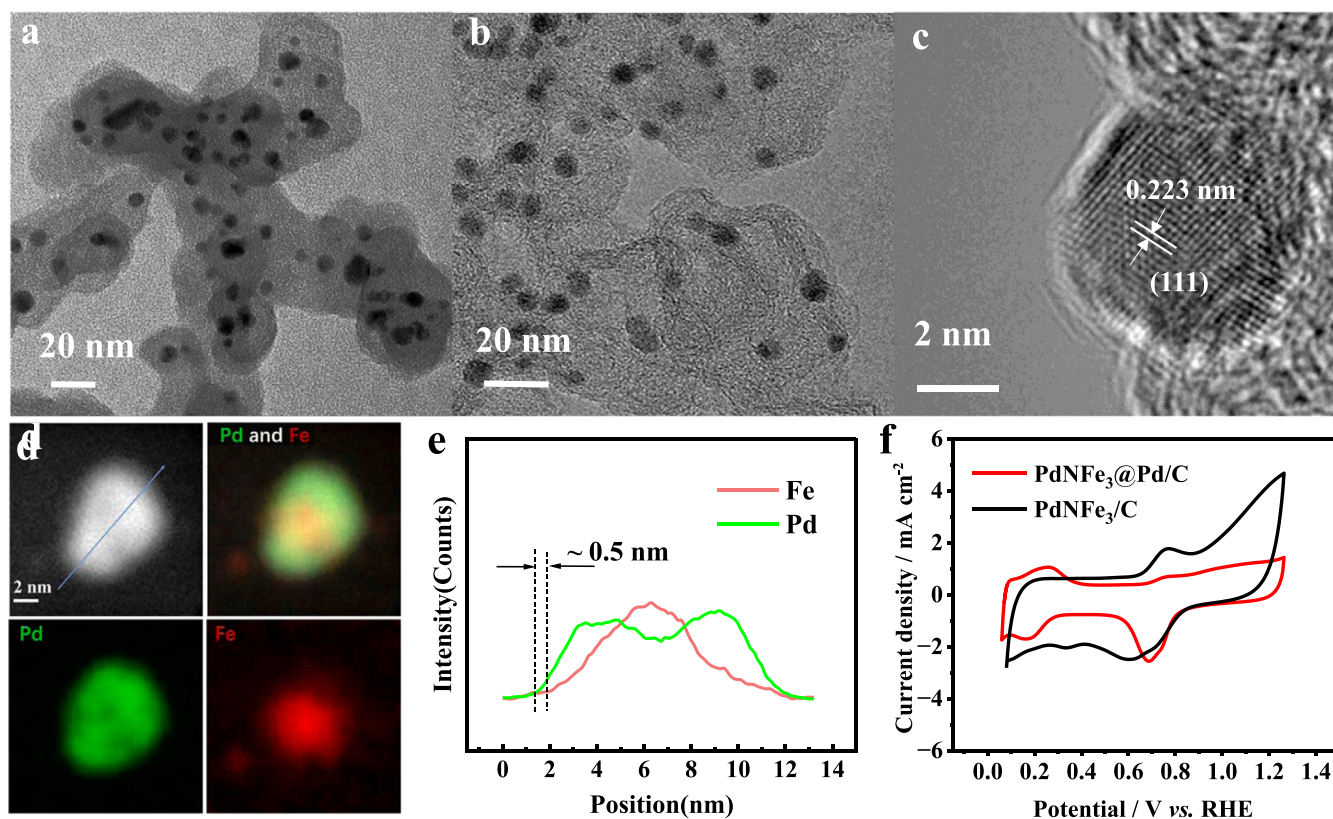To evaluate the catalytic activities of these catalysts toward ORR, the

Fig. 2. (a) TEM images of PdNFe$_3$/C; (b) TEM images of PdNFe$_3$ @Pd/C; (c) HRTEM of individual PdNFe$_3$ @Pd/C nanoparticle; (d) HAADF-STEM and EDS-mapping of PdNFe$_3$ @Pd nanoparticle; (e) EDS-line profile of (d); (f) CV curves of PdNFe$_3$/C and PdNFe$_3$ @Pd/C at a sweep rate of 100 mV s^{-1} collected in N$_2$-saturated 0.1 M HClO$_4$ solution.

ORR polarization curves of these samples were measured in O_2-saturated 0.1 M KOH electrolyte with a scan rate of 10 mV s^{-1}. As shown in Fig. 3a, the onset potential (@0.1 mA cm^{-2}) of PdNFe$_3$@Pd/C is 0.98 V, which is more positive than those on PdNFe$_3$/C, Pd/C and Pt/C, indicating a faster ORR kinetic of PdNFe$_3$@Pd/C. In the mixed kinetic/diffusion regime, the half-wave potentials are usually used as an indicator of the catalytic activity of a catalyst. The PdNFe$_3$@Pd/C catalyst exhibits the highest ORR activity among the evaluated electrocatalysts with a half-wave potential of 0.91 V, a significant 30–60 mV shift to more positive potentials relative to the other three catalysts. The much enhanced activity of PdNFe$_3$@Pd/C compared with PdNFe$_3$/C indicates that the construction of core-shell structure leads to the much-enhanced activity, while the N-doped C has very limited contribution to the unique ORR activity of PdNFe$_3$@Pd/C. The kinetic current (j_k) was calculated using Koutecky-Levich equation (details can be found in experimental section). As seen in Fig. 3b, the PdNFe$_3$@Pd/C catalyst exhibits much higher MA than Pd/C and Pt/C. For instance, PdNFe$_3$@Pd/C catalyst produces current as high as 1.14 A•mg$_{Pd}^{-1}$ at 0.9 V, which is 9-fold and 6-fold higher than Pt/C catalyst (0.12 A mg$_{Pt}^{-1}$) and Pd/C catalyst (0.18 A mg$_{Pd}^{-1}$). The MA of PdNFe$_3$@Pd/C is also superior to most Pd-based catalysts currently reported, as summarized in Table S1. To investigate the effect of composition on activity, the specific activities (SA) of these catalysts were also evaluated. The SA can be obtained by normalizing currents with electrochemically active surface areas (ECSA) that are determined by CO stripping and underpotentially deposited hydrogen (Figs. S6 and S7). The PdNFe$_3$@Pd/C catalyst also exhibits the highest SA of 1.95 mA cm^{-2} at 0.9 V$_{RHE}$, which is ~9 and ~11 times higher than those of Pt/C (0.21 mA cm^{-2}) and Pd/C catalysts (0.17 mA cm^{-2}), respectively. Furthermore, the PdNFe$_3$@Pd/C catalyst still shows the highest MA (4.71 A mg$_{Pd}^{-1}$) and SA (8.02 mA cm^{-2}) among all catalysts at 0.85 V$_{RHE}$, which is consistent with the above tendency at 0.9 V$_{RHE}$. As the important indicator to evaluate the ORR kinetic process of catalyst, Tafel slope was also calculated from ORR polarization curve. As shown in Fig. 3c, PdNFe$_3$@Pd/C catalyst exhibits the relatively smaller slope of 44.38 mV dec^{-1} compared to that of Pd/C and Pt/C, suggesting fast ORR reaction kinetics. Additionally, the

rotating ring-disk electrode (RRDE) measurement was conducted for investigating the oxygen reduction pathways of PdNFe$_3$@Pd/C. As shown in Fig. 3d, the electron transfer number (n) per oxygen molecule for PdNFe$_3$@Pd/C was determined as ~4.0, and the H_2O_2 yield (H_2O_2%) is lower than 10%. The result is further verified by Koutechky-Levich plots (Fig. S8), indicating that the ORR on PdNFe$_3$@Pd/C dominantly proceeds with an efficient four-electron pathway (4e$^-$) and complete conversion of oxygen to water rather than H_2O_2 [41].

The stability of the catalysts was assessed by chronoamperometric measurement in O_2-saturated 0.1 M KOH electrolyte at 0.5 V$_{RHE}$. As shown in Fig. 4a, Continuous oxygen reduction (5.5 h) on PdNFe$_3$@Pd/C electrode cause 9.5% decrease in current density, which is much lower than those for Pt/C (20.1%) and Pd/C (26.3%). After stability measurement, the overall morphology of PdNFe$_3$@Pd/C is well maintained and the average size of nanoparticles is still near 6 nm (Fig. 4b). Furthermore, PdNFe$_3$@Pd/C was applied in rechargeable Zn–air batteries and shows enhanced performance. Fig. 4e and f present the total discharge−charge.

circling curve profiles and the enlarged cycle voltage of PdNFe$_3$@Pd/C + IrO$_2$/C enabled battery. The discharge potential undergoes an only 17-mV decrease from 1.23 V at the first cycle to 1.06 V at the 186th cycle, which is 10 mV lower than that for the Pt/C + IrO$_2$/C-enabled battery (Fig. 4c and d), further illustrating that PdNFe$_3$@Pd/C NPs possess much better performance than the Pt/C catalyst. Moreover, PdNFe$_3$@Pd/C was assemblized into the membrane electrode as a cathode for assessment of the ORR performance in an actual AEMFCs. MEA was fabricated using catalyst-coated membrane method by spraying catalyst ink onto a home-made anion exchanged membrane [27]. As shown in Fig. S9, the PdNFe$_3$@Pd/C-enabled AEMFCs generated a current density of almost 400 mA cm^{-2} at 0.6 V and exhibited a peak power density of 270 mW cm^{-2}. In contract, under the same conditions, the AEMFCs with Pd/C cathode yielded 190 mA cm^{-2} and a low peak power density of 147 mW cm^{-2}. Obviously, PdNFe$_3$@Pd/C still showed enhanced ORR performance even though in the single cell.

To understand the superior ORR performance of PdNFe$_3$@Pd/C, XPS analysis of Pd 3d spectra was conducted. As presented in Fig. 5a, the Pd
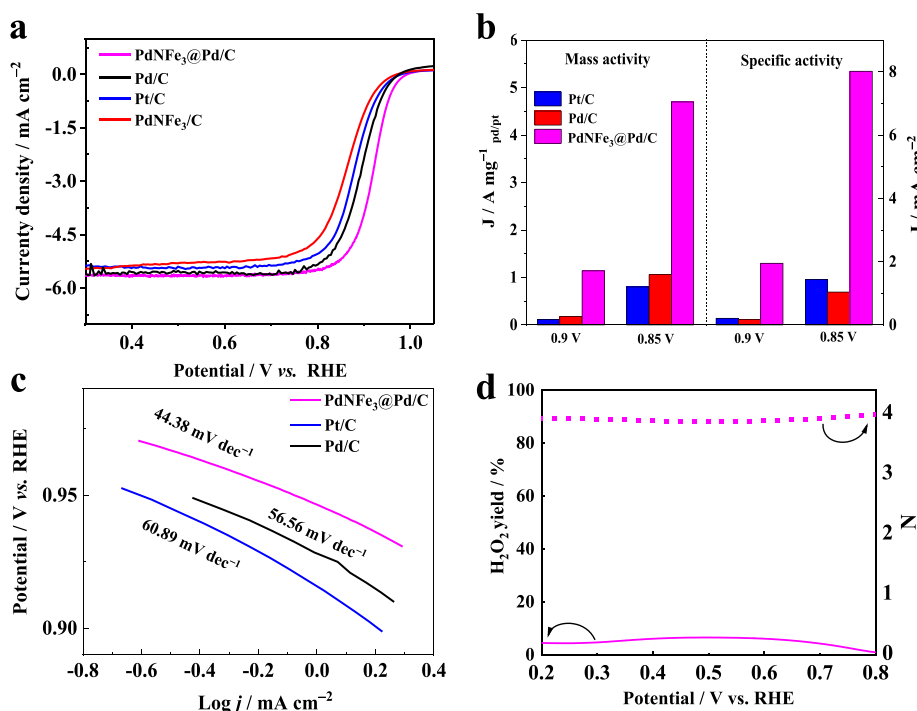

Fig. 3. (a) ORR polarization curves of Pt/C, Pd/C and PdNFe$_3$@Pd/C in O_2-saturated 0.1 M KOH at a rotation rate of 1600 rpm and a scan rate of 10 mV s^{-1}; (b) The comparisons in mass activity and specific activity at 0.9 and 0.85 V$_{RHE}$; (c) Tafel slopes for the catalysts; (d) The peroxide yield and electron transfer numbers.
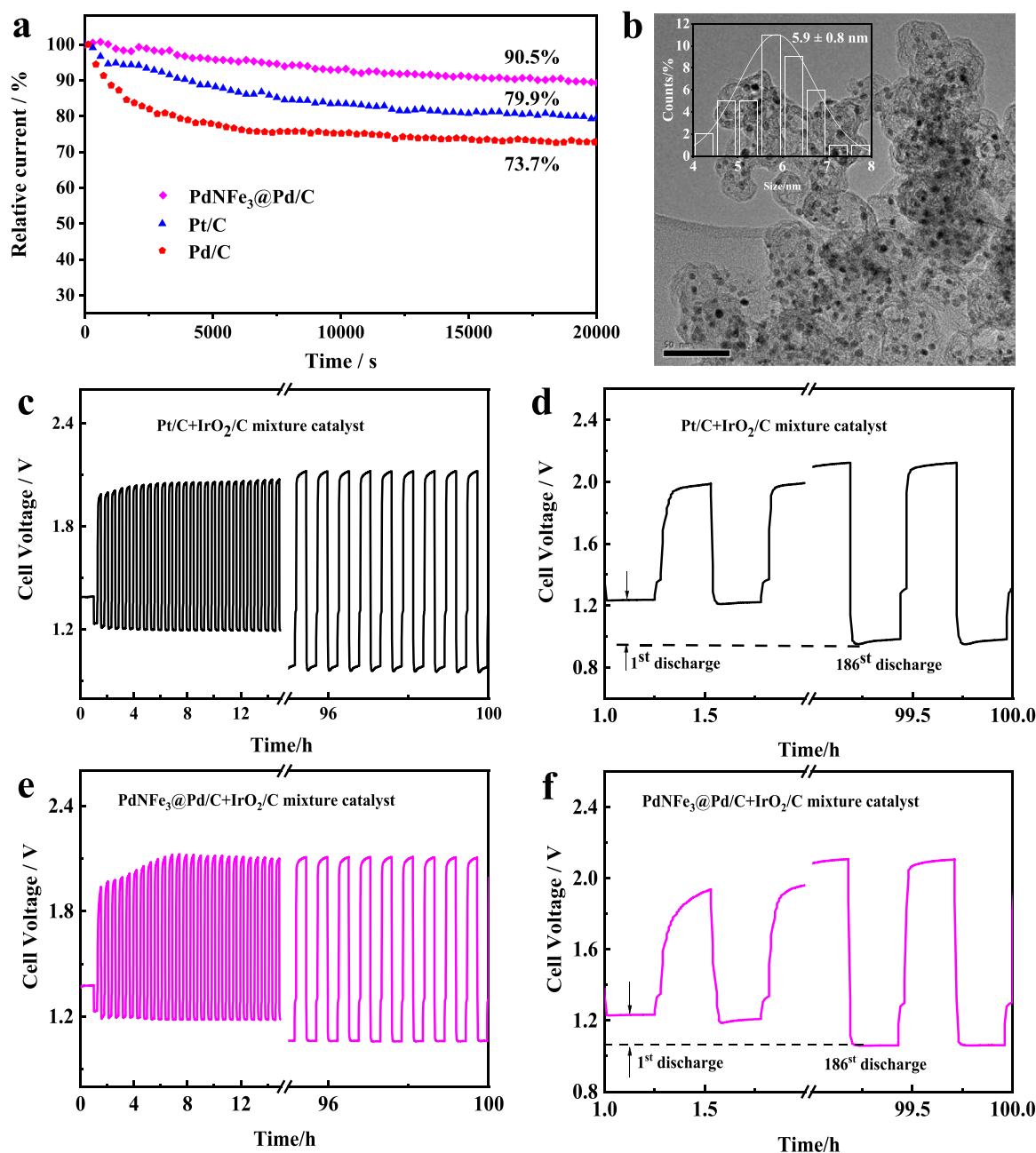
Fig. 4. (a) Chronoamperometric measurements at 0.5 V_{RHE} for the catalysts; (b) TEM image and the sized distribution of PdNFe$_3$@Pd/C after durability test; (c, d) Discharge and charge curves of zinc−air batteries fabricated with Pt/C+IrO$_2$/C; (e, f) Discharge and charge curves of zinc−air batteries fabricated with PdNFe$_3$@Pd/C+ IrO$_2$/C.

3$d_{5/2}$ and Pd 3$d_{3/2}$ peaks of PdNFe$_3$/C and PdNFe$_3$@Pd/C are slightly higher than that of Pd/C. The observed positive shifting indicates a downshift of the d-band center for Pd in the antiperovskite, thus impacting the interaction between Pd and the reactants or intermediates [42,43]. Theoretically, a core-shell model of PdNFe$_3$@Pd(111) with 3 at. layers of Pd as the shell was constructed for DFT calculations (Fig. S11). The atomic thickness of Pd shell was determined according to the results of EDS-line profile analysis above and the simulated PdNFe$_3$@Pd(111) NP (Fig. S10). The Pd−Pd distance is used to evaluate the strain effect at the surface of the PdNFe$_3$@Pd (111) and Pd (111). As shown in Fig. 5b, the average Pd−Pd distance of Pd (111) at PdNFe$_3$@Pd is 2.73 Å, which is 0.06 Å shorter than that of the pure Pd (111), indicating the Pd at PdNFe$_3$@Pd surface has a 2.15% compressive strain. Basically, the compressive strain induced by lattice mismatch will regulate the electronic structure and then influence the adsorption

property on catalyst. Therefore, the d-band center is carried out to further explain the strain effect on ORR performance. As shown in the Fig. 5c, PdNFe$_3$@Pd (111) slab exhibits a significant downshift of the d-band center compared to that of the Pd (111) slab. The down-shift of the d-band center will weaken the surface chemisorption of oxygen-containing intermediates, thereby improving the ORR performance [44]. This is consistent with the XPS results and the negative shift of the CO oxidation peak potentials for PdNFe$_3$@Pd/C compared to Pd/C (Fig. S6). The reaction energy of different steps during ORR was calculated to further understand the enhanced ORR activity. As shown in Fig. 5d, the rate-determined step (RDS) steps of ORR on both catalysts are the third step (*O → *OH), with the overpotentials of 0.81 eV and 0.95 eV, respectively. Obviously, the PdNFe$_3$@Pd exhibits enhanced catalytic activity for ORR compared to that of pure Pd, well agreeing with the experimental observations.
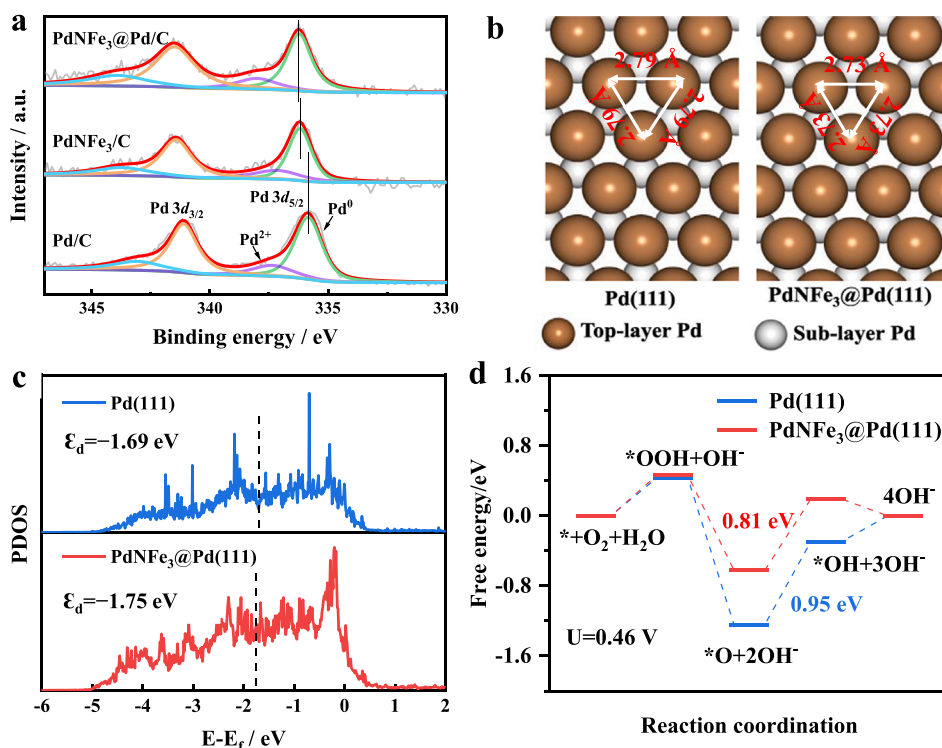
Fig. 5. (a) Pd 3*d* spectra in Pd/C, PdNFe₃/C, and PdNFe₃ @Pd/C; (b) Pd-Pd distence of DFT optmized PdNFe₃ @Pd(111) and Pd(111); (c) Density of States of Pd and PdNFe₃ @Pd. The vertical line denotes d-band center of corresponding catalysts; (d) The free energies of intermediates along the ORR reaction pathway on Pd (111) and PdNFe₃ @Pd (111).

4. Conclusions

In summary, we have successfully developed a new and cost-effective catalytic material of antiperovskite PdNFe₃ and constructed a high performance PdNFe₃ @Pd catalyst with atomic layers of strained Pd shell. The as-prepared PdNFe₃ @Pd/C with small particle size of ~6 nm presents a high MA of 1.14 A mg$_{Pd}^{-1}$ at 0.9 V, which is 9 and 6 times higher than those of the Pt/C and Pd/C, respectively. Besides, the PdNFe₃ @Pd/C shows a current retention of 90.5% after long term stability test, which is much higher that those of Pt/C. DFT calculations reveal that the Pd at PdNFe₃ @Pd surface has a 2.15% compressive strain induced by lattice mismatch between core and shell. The compressive strain results in the down-shift of the d-band center and weakens the surface chemisorption of oxygen-containing intermediates on PdNFe₃ @Pd, which further decreasing the reaction energy barrier of ORR rate-determining step. Meanwhile, the durable core is favorable for the structure stability and catalytic stability of the catalyst. More importantly, the excellent performance of PdNFe₃ @Pd/C was also verified in AEMFCs and rechargeable Zn−air batteries. This work opens an avenue to develop highly efficient electrocatalysts with low-content of Pd for energy storage and conversion devices.

CRediT authorship contribution statement

Jiamin Liu: Conceptualization, Methodology, Data curation, Writing – original draft. **Longhai Zhang:** Investigation, Software, Validation, Writing – review & editing. **Jiaye Liu:** Investigation, Writing – review & editing. **Zhihang Xu:** Investigation, Writing – review & editing. **Jiaxi Zhang:** Writing – review & editing. **Lecheng Liang:** Software. **Li Du:** Supervision, Investigation. **Huiyu Song:** Methodology, Visualization. **Ye Zhu:** Methodology, Supervision. **Nanwen Li:** Methodology, Supervision, Funding acquisition. **Zhiming Cui:** Conceptualization, Methodology, Supervision, Investigation, Funding acquisition, Resources, Data curation, Writing – review & editing.

Declaration of Competing Interest

The authors declare that they have no known competing financial interests or personal relationships that could have appeared to influence the work reported in this paper.

Data availability

Data will be made available on request.

Acknowledgements

Appendix A. Supporting information

Supplementary data associated with this article can be found in the online version at doi:10.1016/j.apcatb.2023.122807.

References

[1] Y. Yang, C.R. Peltier, R. Zeng, R. Schimmenti, Q. Li, X. Huang, Z. Yan, G. Potsi, R. Selhorst, X. Lu, W. Xu, M. Tader, A.V. Soudackov, H. Zhang, M. Krumov, E. Murray, P. Xu, J. Hitt, L. Xu, H.Y. Ko, B.G. Ernst, C. Bundschu, A. Luo, D. Markovich, M. Hu, C. He, H. Wang, J. Fang, R.A. DiStasio Jr., L.F. Kourkoutis, A. Singer, K.J.T. Noonan, L. Xiao, L. Zhuang, B.S. Pivovar, P. Zelenay, E. Herrero, J. M. Feliu, J. Suntivich, E.P. Giannelis, S. Hammes-Schiffer, T. Arias, M. Mavrikakis, T.E. Mallouk, J.D. Brock, D.A. Muller, F.J. DiSalvo, G.W. Coates, H.D. Abruna, Electrocatalysis in alkaline media and alkaline membrane-based energy technologies, Chem. Rev. 122 (2022) 6117–6321, https://doi.org/10.1021/acs.chemrev.1c00331.
[2] F. Xiao, Y.C. Wang, Z.P. Wu, G. Chen, F. Yang, S. Zhu, K. Siddharth, Z. Kong, A. Lu, J.C. Li, C.J. Zhong, Z.Y. Zhou, M. Shao, Recent advances in electrocatalysts for

proton exchange membrane fuel cells and alkaline membrane fuel cells, Adv. Mater. 33 (2021), e2006292, https://doi.org/10.1002/adma.202006292.

[3] S. Zhang, Q. Zhou, L. Fang, R. Wang, T. Lu, Q. Zhao, X. Gu, S. Tian, L. Xu, H. Pang, Gram-scale synthesis and unraveling the activity origin of atomically dispersed Co-N_4O sites toward superior electrocatalytic oxygen reduction, Appl. Catal. B 328 (2023), 122489, https://doi.org/10.1016/j.apcatb.2023.122489.

[4] C. Shao, L. Wu, Y. Wang, K. Qu, H. Chu, L. Sun, J. Ye, B. Li, X. Wang, Engineering asymmetric Fe coordination centers with hydroxyl adsorption for efficient and durable oxygen reduction catalysis, Appl. Catal. B 316 (2022), 121607, https://doi.org/10.1016/j.apcatb.2022.121607.

[5] T. Wang, A. Chutia, D.J.L. Brett, P.R. Shearing, G. He, G. Chai, I.P. Parkin, Palladium alloys used as electrocatalysts for the oxygen reduction reaction, Energy Environ. Sci. 14 (2021) 2639–2669, https://doi.org/10.1039/D0EE03915B.

[6] L. Jiang, A. Hsu, D. Chu, R. Chen, Size-dependent activity of palladium nanoparticles for oxygen electroreduction in alkaline solutions, J. Electrochem. Soc. 156 (2009) B643, https://doi.org/10.1149/1.3098478.

[7] W. Jiao, C. Chen, W. You, X. Zhao, J. Zhang, Y. Feng, P. Wang, R. Che, Hollow palladium-gold nanochains with periodic concave structures as superior ORR electrocatalysts and highly efficient SERS substrates, Adv. Energy Mater. 10 (2020) 1904072, https://doi.org/10.1002/aenm.201904072.

[8] H. Wang, W. Wang, H. Yu, Q. Mao, Y. Xu, X. Li, Z. Wang, L. Wang, Interface engineering of polyaniline-functionalized porous Pd metallene for alkaline oxygen reduction reaction, Appl. Catal. B 307 (2022), 121172, https://doi.org/10.1016/j.apcatb.2022.121172.

[9] J.A. Zamora Zeledon, M.B. Stevens, G. Gunasooriya, A. Gallo, A.T. Landers, M. E. Kreider, C. Hahn, J.K. Norskov, T.F. Jaramillo, Tuning the electronic structure of Ag-Pd alloys to enhance performance for alkaline oxygen reduction, Nat. Commun. 12 (2021) 620, https://doi.org/10.1038/s41467-021-20923-z.

[10] H. Wang, W. Luo, L. Zhu, Z. Zhao, B.E. W, X. Tu, M. Ke, C. Sui, Q. Chen, Y. Chen, Y. Li, Huang, Synergistically enhanced oxygen reduction electrocatalysis by subsurface atoms in ternary PdCuNi alloy catalysts, Adv. Funct. Mater. 28 (2018) 1707219, https://doi.org/10.1002/adfm.201707219.

[11] H. Lv, D. Xu, L. Sun, J. Henzie, S.L. Suib, Y. Yamauchi, B. Liu, Ternary palladium–boron–phosphorus alloy mesoporous nanospheres for highly efficient electrocatalysis, ACS Nano 13 (2019) 12052–12061, https://doi.org/10.1021/acsnano.9b06339.

[12] Z.P. Wu, S. Shan, S.Q. Zang, C.J. Zhong, Dynamic core-shell and alloy structures of multimetallic nanomaterials and their catalytic synergies, Acc. Chem. Res. 53 (2020) 2913–2924, https://doi.org/10.1021/acs.accounts.0c00564.

[13] S. Maiti, K. Maiti, M.T. Curnan, K. Kim, K.-J. Noh, J.W. Han, Engineering electrocatalyst nanosurfaces to enrich the activity by inducing lattice strain, Energy Environ. Sci. 14 (2021) 3717–3756, https://doi.org/10.1039/D1EE00074H.

[14] C. Tang, N. Zhang, Y. Ji, Q. Shao, Y. Li, X. Xiao, X. Huang, Fully tensile strained Pd_3Pb/Pd tetragonal nanosheets enhance oxygen reduction catalysis, Nano Lett. 19 (2019) 1336–1342, https://doi.org/10.1021/acs.nanolett.8b04921.

[15] P. Wang, Y. Luo, G. Zhang, Z. Chen, H. Ranganathan, S. Sun, Z. Shi, Interface engineering of Ni_xS_y@ MnO_xH_y nanorods to efficiently enhance overall-water-splitting activity and stability, Nano-Micro Lett. 14 (2022) 120, https://doi.org/10.1007/s40820-022-00860-2.

[16] G. Wang, J. Guan, L. Xiao, B. Huang, N. Wu, J. Lu, L. Zhuang, Pd skin on AuCu intermetallic nanoparticles: A highly active electrocatalyst for oxygen reduction reaction in alkaline media, Nano Energy 29 (2016) 268–274, https://doi.org/10.1016/j.nanoen.2016.04.005.

[17] S. Mondal, C.R. Raj, Electrochemical dealloying-assisted surface-engineered Pd-based bifunctional electrocatalyst for formic acid oxidation and oxygen reduction, ACS Appl. Mater. Interfaces 11 (2019) 14110–14119, https://doi.org/10.1021/acsami.9b00589.

[18] D. Wang, H.L. Xin, H. Wang, Y. Yu, E. Rus, D.A. Muller, F.J. DiSalvo, H.D. Abruña, Facile Synthesis of Carbon-Supported Pd–Co Core–Shell Nanoparticles as Oxygen Reduction Electrocatalysts and Their Enhanced Activity and Stability with Monolayer Pt Decoration, Chem. Mater. 24 (2012) 2274–2281, https://doi.org/10.1021/cm203863d.

[19] M. Zhou, C. Li, J. Fang, Noble-metal based random alloy and intermetallic nanocrystals: syntheses and applications, Chem. Rev. 121 (2020) 736–795, https://doi.org/10.1021/acs.chemrev.0c00436.

[20] D. Sun, Y. Wang, K.J.T. Livi, C. Wang, R. Luo, Z. Zhang, H. Alghamdi, C. Li, F. An, B. Gaskey, T. Mueller, A.S. Hall, Ordered intermetallic Pd_3Bi prepared by an electrochemically induced phase transformation for oxygen reduction electrocatalysis, ACS Nano 13 (2019) 10818–10825, https://doi.org/10.1021/acsnano.9b06019.

[21] Z. Cui, L. Li, A. Manthiram, J.B. Goodenough, Enhanced cycling stability of hybrid Li–air batteries enabled by ordered Pd_3Fe intermetallic electrocatalyst, J. Am. Chem. Soc. 137 (2015) 7278, https://doi.org/10.1021/jacs.5b03865.

[22] J. Li, S. Sun, Intermetallic nanoparticles: synthetic control and their enhanced electrocatalysis, Acc. Chem. Res. 52 (2019) 2015–2025, https://doi.org/10.1021/acs.accounts.9b00172.

[23] Z. Cui, H. Chen, W. Zhou, M. Zhao, F.J. DiSalvo, Structurally ordered Pt_3Cr as oxygen reduction electrocatalyst: ordering control and origin of enhanced stability, Chem. Mater. 27 (2015) 7538–7545, https://doi.org/10.1021/acs.chemmater.5b03912.

[24] J.T.L. Gamler, H.M. Ashberry, S.E. Skrabalak, K.M. Koczkur, Random alloyed versus intermetallic nanoparticles: a comparison of electrocatalytic performance, Adv. Mater. 30 (2018), e1801563, https://doi.org/10.1002/adma.201801563.

[25] J. Zhang, L. Zhang, Z. Cui, Strategies to enhance the electrochemical performances of Pt-based intermetallic catalysts, Chem. Commun. 57 (2021) 11–26, https://doi.org/10.1039/D0CC05170E.

[26] A. Jain, S.P. Ong, G. Hautier, W. Chen, W.D. Richards, S. Dacek, S. Cholia, D. Gunter, D. Skinner, G. Ceder, K.A. Persson, Commentary: The Materials Project: A materials genome approach to accelerating materials innovation, APL Mater. 1 (2013), 011002, https://doi.org/10.1063/1.4812323.

[27] J. Wang, Y. Zhao, B.P. Setzler, S. Rojas-Carbonell, C. Ben Yehuda, A. Amel, M. Page, L. Wang, K. Hu, L. Shi, Poly (aryl piperidinium) membranes and ionomers for hydroxide exchange membrane fuel cells, Nat. Energy 4 (2019) 392–398, https://doi.org/10.1038/s41560-019-0372-8.

[28] G. Kresse, J. Furthmüller, Efficient iterative schemes for ab initio total-energy calculations using a plane-wave basis set, J. Phys. Rev. B 54 (1996) 11169, https://doi.org/10.1103/PhysRevB.54.11169.

[29] P.E. Blochl, Projector augmented-wave method, Phys. Rev. B 50 (1994) 17953–17979, https://doi.org/10.1103/PhysRevB.50.17953.

[30] J.P. Perdew, K. Burke, M. Ernzerhof, Generalized gradient approximation made simple, Phys. Rev. Lett. 77 (1996) 3865, https://doi.org/10.1103/PhysRevLett.77.3865.

[31] H.J. Monkhorst, J.D. Pack, Special points for Brillouin-zone integrations, Phys. Rev. B 13 (1976) 5188–5192, https://doi.org/10.1103/PhysRevB.13.5188.

[32] Y. Jiao, Y. Zheng, M. Jaroniec, S.Z. Qiao, Origin of the electrocatalytic oxygen reduction activity of graphene-based catalysts: a roadmap to achieve the best performance, J. Am. Chem. Soc. 136 (2014) 4394–4403, https://doi.org/10.1021/ja500432h.

[33] Q. Lv, W. Si, J. He, L. Sun, C. Zhang, N. Wang, Z. Yang, X. Li, X. Wang, W. Deng, Y. Long, C. Huang, Y. Li, Selectively nitrogen-doped carbon materials as superior metal-free catalysts for oxygen reduction, Nat. Commun. 9 (2018) 3376, https://doi.org/10.1038/s41467-018-05878-y.

[34] Z. Cui, H. Chen, M. Zhao, D. Marshall, Y. Yu, H. Abruna, F.J. DiSalvo, Synthesis of structurally ordered Pt_3Ti and Pt_3V nanoparticles as methanol oxidation catalysts, J. Am. Chem. Soc. 136 (2014) 10206–10209, https://doi.org/10.1021/ja504573a.

[35] Z. Cui, H. Chen, W. Zhou, M. Zhao, F.J. DiSalvo, Structurally ordered Pt_3Cr as oxygen reduction electrocatalyst: ordering control and origin of enhanced stability, Chem. Mater. 27 (2015) 7538–7545, https://doi.org/10.1021/acs.chemmater.5b03912.

[36] Z. Cui, L. Li, A. Manthiram, J.B. Goodenough, Enhanced cycling stability of hybrid Li-air batteries enabled by ordered Pd_3Fe intermetallic electrocatalyst, J. Am. Chem. Soc. 137 (2015) 7278–7281, https://doi.org/10.1021/jacs.5b03865.

[37] Z. Cui, H. Chen, M. Zhao, F.J. DiSalvo, High-performance Pd_3Pb intermetallic catalyst for electrochemical oxygen reduction, Nano Lett. 16 (2016) 2560–2566, https://doi.org/10.1021/acs.nanolett.6b00121.

[38] J. Li, Z. Xi, Y.T. Pan, J.S. Spendelow, P.N. Duchesne, D. Su, Q. Li, C. Yu, Z. Yin, B. Shen, Y.S. Kim, P. Zhang, S. Sun, Fe Stabilization by Intermetallic $L1_0$-FePt and Pt Catalysis Enhancement in $L1_0$-FePt/Pt Nanoparticles for Efficient Oxygen Reduction Reaction in Fuel Cells, J. Am. Chem. Soc. 140 (2018) 2926–2932, https://doi.org/10.1021/jacs.7b12829.

[39] M. Xie, Z. Lyu, R. Chen, M. Shen, Z. Cao, Y. Xia, Pt-Co@Pt Octahedral Nanocrystals: Enhancing Their Activity and Durability toward Oxygen Reduction with an Intermetallic Core and an Ultrathin Shell, J. Am. Chem. Soc. 143 (2021) 8509–8518, https://doi.org/10.1021/jacs.1c04160.

[40] Z. Li, H. Jang, D. Qin, X. Jiang, X. Ji, M.G. Kim, L. Zhang, X. Liu, J. Cho, Alloy-strain-output induced lattice dislocation in Ni_3FeN/Ni_3Fe ultrathin nanosheets for highly efficient overall water splitting, J. Mater. Chem. A 9 (2021) 4036–4043, https://doi.org/10.1039/D0TA11618A.

[41] W. Zhang, J. Chang, Y. Yang, Strong precious metal–metal oxide interaction for oxygen reduction reaction: a strategy for efficient catalyst design, SusMat 3 (2023) 2–20, https://doi.org/10.1002/sus2.108.

[42] M. Luo, Z. Zhao, Y. Zhang, Y. Sun, Y. Xing, F. Lv, Y. Yang, X. Zhang, S. Hwang, Y. Qin, J.Y. Ma, F. Lin, D. Su, G. Lu, S. Guo, PdMo bimetallene for oxygen reduction catalysis, Nature 574 (2019) 81–85, https://doi.org/10.1038/s41586-019-1603-7.

[43] M. Wakisaka, S. Mitsui, Y. Hirose, K. Kawashima, H. Uchida, M. Watanabe, Electronic structures of Pt-Co and Pt-Ru alloys for CO-tolerant anode catalysts in polymer electrolyte fuel cells studied by EC-XPS, J. Phys. Chem. B 110 (2006) 23489–23496, https://doi.org/10.1021/jp0653510.

[44] E. Christoffersen, P. Liu, A. Ruban, H.L. Skriver, J.K. Nørskov, Anode materials for low-temperature fuel cells: a density functional theory study, J. Catal. 199 (2001) 123–131, https://doi.org/10.1006/jcat.2000.3136.